Nanocrystalline B/C/S-Doped ZnO-SnO₂ Photocatalysts: Preparation, Characterization and Photocatalytic Performance

S.R. Kande[1], U.G. Ghoshir[1], J.K. Khedkar[2], G.G. Muley[3] and A.B. Gambhire[4,*]

[1]Research Centre, Department of Chemistry, New Arts, Commerce and Science College, Ahmednagar-414001, India
[2]Department of Chemistry, New Arts, Commerce and Science College, Shevgaon-414502, India
[3]Department of Physics, Sant Gadge Baba Amravati University, Amravati-444602, India
[4]Department of Chemistry, Shri Anand College, Pathardi-414102, India

*Corresponding author: Fax: +91 2428 223033; Tel.: +91 2428 222736; E-mail: abg_chem@ymail.com

Boron (B), carbon (C) and sulphur (S) doped ZnO-SnO₂ were successfully prepared by facile precipitation method. As prepared nanocomposite photocatalyst was characterized by X-ray diffraction, X-ray photoelectron spectroscopy, scanning electron microscopy, high resolution transmission electron spectroscopy, Fourier transform infrared spectroscopy, photoluminescence spectra, UV-diffuse reflectance spectra and BET surface area measurement. The photocatalytic activity of prepared nanocomposite photocatalysts was studied by degradation of methyl orange dye under natural sunlight irradiation. S-doped ZnO-SnO₂ was found to be more efficient than that of B,C-doped ZnO-SnO₂ and bare ZnO-SnO₂ nanocomposites. The photocatalytic activity of prepared photocatalysts follows trend as: S-doped ZnO-SnO₂ > C-doped ZnO-SnO₂ > B-doped ZnO-SnO₂ > pure ZnO-SnO₂. The enhanced activity of prepared photocatalysts could be attributed to the high specific surface area and small particle size.

Keywords: Doped nanocomposites, Dye degradation, Photocatalysis.

INTRODUCTION

The demineralization of various toxic contaminants in wastewater using solar light has attracted different researchers. The byproducts and wastewater discharged through various industries contain high concentration of toxic materials [1]. Due to growing industrialization, the contaminated water with such toxic waste has already aggravated the situation by affecting health of living beings. In this regard, an intensive research on the development of nanocomposite with optimum photocatalytic activity has been pursued by different research groups. These nanocomposites have attracted researchers significantly due to their unique optical, electronic and chemical properties arising from the synergistic effect of metal oxides in photocatalytic activity. Accordingly, several metal oxides such as TiO₂, ZnO, WO₃, Mo₂O₃, V₂O₅, Bi₂O₃, Fe₃O₄ and SnO₂ [2-9] have been demonstrated as a successful alternative to the various conventional methods for the remediation of environmental problems. Electron-hole (e-h) pairs get generated after UV

light irradiation on photocatalyst that further promotes formation of •OH radicals (reactive species) which is advanced oxidation process and prominent technique for complete mineralization of toxic organic pollutants in industrial wastewater. However, the photocatalytic efficiency of photocatalyst decreases by the e-h pair recombination to that of interfacial charge transfer. To overcome this problem two metal oxide semiconductor particles with different ionization potential, band energy levels and different electron affinities are coupled. After irradiation the photo-induced electrons get excited from valence band to conduction band. These excited electrons further get transferred to the conduction band of the metal oxide semiconductor with lower energy. Simultaneously, the photogenerated holes are migrated in opposite direction from lower valence band to higher valence band. This results in separation of e-h pair which further decreases the recombination rate. Accordingly the various combinations of different metal oxide semiconductors like ZnO-In₂O₃ [10], CeO₂-SnO₂ [11], TiO₂-WO₃ [12], NiO-SnO₂ [13], ZnO-Cr₂O₃ [14], TiO₂-Fe₂O₃ [15]

and ZnO-SnO₂ [16] have been investigated. Among several studied metal oxides, ZnO and SnO₂ found very active in presence of solar energy. The matching energy levels, ease of synthesis, high electron mobility, non-toxicity, low crystallization temperature and low cost are some of the peculiarities of ZnO and SnO₂ those have attracted the researchers. The surface of both metal oxides is commonly used as a sink of vacancies. The oxygen deficiencies in pure state of ZnO and SnO₂ are low and can be increased by doping method. Also the quantum efficiency of these metal oxides is less due to high rate of e-h pair recombination and large band gap. Pertaining to this, the literature reports the enhanced photocatalytic activity by coupling of ZnO and SnO₂ metal oxides. Such composites have already found their applications in solar cells, transistors, lithium ion batteries and photocatalysis [17]. However, the undoped ZnO-SnO₂ nanocomposite still could not able to shift the absorption to visible region. The continuous efforts have been made to change the optoelectronic properties of semiconductor nanocomposites by addition of small quantity of dopant that alters the regular arrangement of crystal lattice. Among such dopants, the addition of nonmetals on metal oxides decreases both the band gap energy and e-h pair recombination by the formation of mid gap energy states as well as increasing the quantity of defects into the crystal lattice of metal oxides [18-24]. Carbon, boron and sulphur, especially act as active doping elements and enhance the photocatalytic activity of nanocomposite [25-27]. According to literature survey most of the study were concluded in combination of different metal oxide semiconductor doped with metal or nonmetals. Doping of C, B and S on ZnO-SnO₂ yet not been evaluated and reported in the literature.

Thus, the present work deals with the successful synthesis of B, C and S-doped ZnO-SnO₂ nanocomposite photocatalyst by precipitation method. The results show the least particle size and highest photocatalytic activity for S-doped ZnO-SnO₂.

EXPERIMENTAL

All the chemicals (zinc nitrate, stannic chloride, ethylene glycol, sodium hydroxide, ammonia, thiourea, boric acid) used for the preparation of B/C/S-doped ZnO-SnO₂ nanocomposites were analytical grade and purchased from Merck so used without further purification.

Synthesis of doped B/C/S ZnO-SnO₂ nanocomposites: B/C/S-doped ZnO-SnO₂ nanocomposites were synthesized by using precipitation method. Zinc nitrate (0.5 M, 100 mL) and stannic chloride was added into 500 mL beaker along with 20 mL 10% ethyl alcohol and 2 mL conc. HNO₃ and stirred for 1 h, followed by the addition of 0.1M carbon, boron and sulphur source. Citric acid/ethylene glycol, boric acid and thiourea were taken as a source of carbon, boron and sulphur, respectively for the preparation of C/B/S-doped ZnO-SnO₂, separately. The pH of the resultant mixture was adjusted to 7 by using 0.1M NaOH to get the precipitate. The mixture was further stirred for another 12 h and then left for aging next 5 days. Then it was evaporated at 80 °C to get powder which is further crushed and calcined at 450 °C for 2 h. The obtained powder was used for dye degradation study and characterization.

Characterization: X-ray diffraction (XRD) for phase purity and structure determination was performed on Brucker D8 Advance diffractometer with CuK$_\alpha$ as radiation source (λ = 1.1506) at a scan rate 0.03º s⁻¹. The morphology, particle size and composition of prepared nanophotocatalysts were studied by using field emission scanning electron microscope (Nova nanoSEM NPEP303). FT-IR spectrum was recorded on Avatar-330 spectrophotometer in the range of 4000-400 cm⁻¹. The microstructure were studied by using Technai F30 HRTEM, FEG field emission transmission electron microscope (TEM) working at 300kV. A UV-Vis diffuse reflectance spectrum (UV-DRS) was carried out using PE LAMBDA35 spectrophotometer in the range of 200-800 nm. Photoluminescence emission spectra (PL) was employed to study the e-h pair recombination and recorded at excitation energy 325 nm on photoluminescence, SCINCO FluoroMate FS-2 using 3 nm slit width at room temperature. Raman spectra were recorded on Renishaw InVia Raman spectrometer using a 532 nm argon ion laser from 100-2000 nm. Chemical composition and valence band spectra of nanocomposites were studied using X-ray photoelectron spectroscopy using (XPS; ESCA-3000, VG Microtech, Uckfield, UK). To study the specific area of prepared samples, nitrogen adsorption/desorption measurement at 77 K on the basis of BET equation were done using Micrometrics ASAP 2020 systems.

Photocatalytic study: Photocatalytic activity of series of doped and undoped ZnO-SnO₂ samples were studied by using degradation of methyl orange under natural sunlight irradiation. The solar light used for irradiation was isolated and measured by UV irradiance meter in the range of 370-500 nm and found to be 26.15 W/m₂ in average. The photocatalytic dye degradation study was performed from 1 p.m. - 2 p.m. in the month of May 2017. The experiment was carried out in 250 mL glass beaker containing 100 mL aqueous solution of methyl orange (50 mg/L). Prepared photocatalyst (0.025 g) was added into the above aquous methyl orange solution with stirring at room temperature. In order to form equilibrium between methyl orange and sample photocatalyst the mixture was stirred continuously in the dark for 60 min. After attaining of equilibrium the beaker was exposed to sunlight. Then 5 mL dye suspension from glass beaker was collected by using syringe after the interval of every 10 min. The sample from collected suspension was removed by filtration through Millipore filter. The decrease in the concentration of methyl orange in the suspension was studied by using UV-visible spectrophotometer at λ_{max} = 507 nm. The degradation efficiency of methyl orange was studied using following expression:

$$\text{Degradation efficiency (\%)} = \frac{C_o - C}{C_o} \times 100$$

where, C_o and C are absorbance of methyl orange prior and after the irradiation of sunlight.

RESULTS AND DISCUSSION

XRD analysis: The samples were characterized by XRD technique in order to study the crystal structure and phase purity of prepared undoped and doped ZnO-SnO₂ nanocomposite. Fig. 1 shows the diffraction pattern of these photocatalysts with several sharp peaks. The peaks at 2θ = 30.7º, 34.3º, 47.8º, 67.9º are well assigned as 100, 002, 110 and 201, respectively, are in good agreement with the standard pattern for hexagonal wurtzite structure of ZnO (JCPDS file No.: 36-1451) [28].
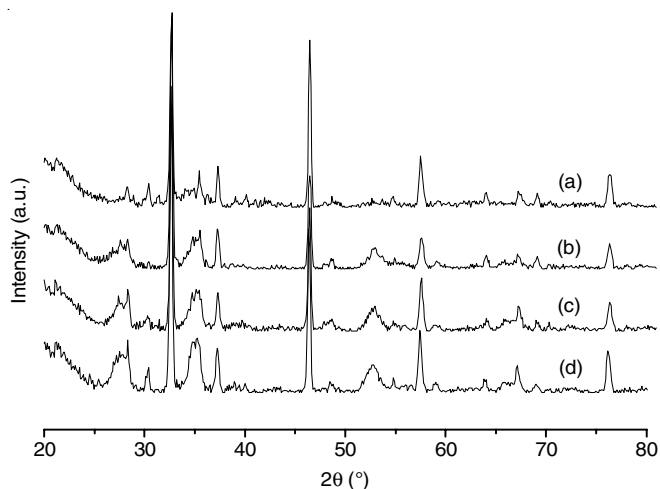
Fig. 1.   XRD patterns of undoped ZnO-SnO_2, B-doped ZnO-SnO_2, C-doped ZnO-SnO_2 and S-doped ZnO-SnO_2 calcined at 450 °C for 2 h in air

Further, additional peaks at 2θ = 27.02º, 33.8º, 38.1º, 52.1º, 57.98º are assigned as 110, 101, 200, 211 and 002, respectively corresponded to the rutile tetragonal structure of SnO_2 (JCPDS file No.: 41-1445) [29]. All the sharp and intense peaks in the diffraction pattern indicate the well crystalline nature of samples. The peaks corresponding to non-metal (B, C and S) dopant were not appeared in XRD pattern. This confirms the successful doping of S on nanocomposite, low concentration of dopant and single phase of synthesized samples [30]. The increased crystalline size of undoped to B/C and S-doped ZnO-SnO_2 was calculated by using Scherrer's equation as shown in Table-1. The calculated crystalline size is in good agreement with the size observed in TEM study.

TABLE-1
MORPHOLOGICAL AND STRUCTURAL PROPERTIES OF
UNDOPED AND B/C/S-doped ZnO-SnO_2 NANOCOMPOSITES

Sample	Particle size (nm)	Surface area (S_{BET}) = $(m^2\ g^{-1})$	Band gap energy (eV)
Pure ZnO-SnO_2	35.6	21.5	2.84
B-doped ZnO-SnO_2	28.5	37.7	2.82
C-doped ZnO-SnO_2	16.3	59.9	2.79
S-doped ZnO-SnO_2	9.2	69.1	2.74

*Pore size was calculated by BJH theory, BET technique was used to study surface area of nanocomposite and band gap energy was estimated using UV-DRS.

FT-IR analysis: Fig. 2 depicts the typical FT-IR spectra of series of undoped and B/C/S-doped ZnO-SnO_2 nanocomposites within range 4000-400 cm^{-1}. The observed peaks of absorbed water molecules at 3459 and 1640 cm^{-1} correspond to OH stretching and bending vibration mode, respectively. The peak intensity gets increased from undoped to S-doped ZnO-SnO_2. The spectra also revealed the Zn−O (520 cm^{-1}) and Sn−O (669 cm^{-1}) stretching modes [31,32]. The remarkable absorption peak of SO_4^{2-} at 1100 cm^{-1} in S-doped ZnO-SnO_2 indicates the formation of S−O bond in the nanocomposite [33]. The characteristic absorption peak at 800 cm^{-1} suggests the existence of bridged Zn−O−Zn, Sn−O−Zn and Sn−O−Sn bond [34].

SEM analysis: It is well known that photocatalytic activity mostly depends on the surface morphology and structure of
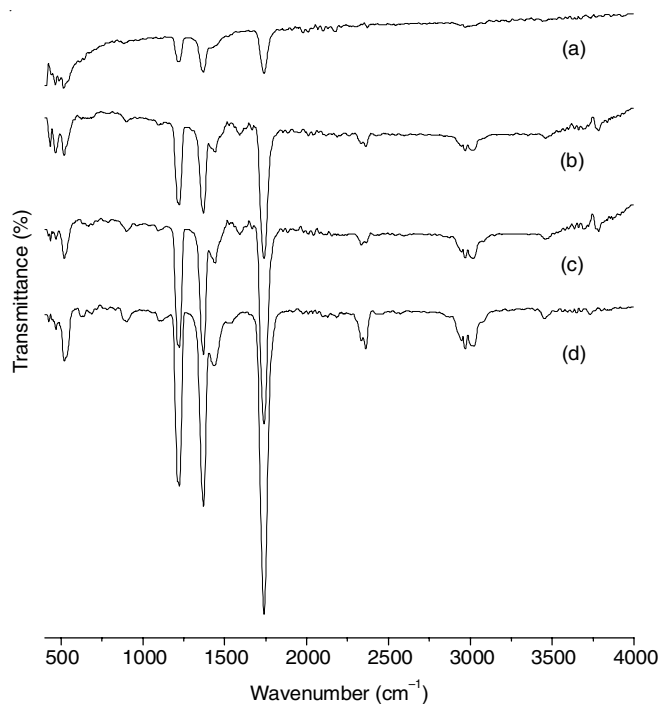

Fig. 2.   FT-IR spectra of (a) pure ZnO-SnO_2, (b) B-doped ZnO-SnO_2, (c) C-doped ZnO-SnO_2 and (d) S-doped ZnO-SnO_2

nanocomposite. Accordingly, we studied the surface morphology of synthesized undoped and B/C/S-doped ZnO-SnO_2 using scanning electron microscope. The corresponding high resolution SEM images shown in Fig. 3a-d revealed the significant structural differences for both doped and undoped ZnO-SnO_2 nanocomposites. The agglomerated spherical crystals were observed in case of undoped ZnO-SnO_2 nanocomposites (Fig. 3a) whereas, B-doped ZnO-SnO_2 (Fig. 3b) developed flower like morphology. C-doped ZnO-SnO_2 shows (Fig. 3c) crushed dry leaves like structure. In case of S-doped ZnO-$SnO2$ the artificial flower made by broken wood pieces type of structure is observed (Fig. 3d). EDX spectrum shown in Fig. 3e clearly revealed the purity of sample and showed presence of S, Zn and Sn in the nanocomposite.

TEM analysis: The morphological study of series of doped and undoped ZnO-SnO_2 was carried out using TEM and HRTEM images as shown in Fig. 4a-f. The particles in undoped ZnO-SnO_2, B-doped ZnO-SnO_2 and C-doped ZnO-SnO_2 appeared as nanorods with agglomeration (Fig. 4a-d). The observed interplanar distances (Fig. 4e) 2.79 and 2.59 Å indicates the (1 0 0) and (0 0 2) plane of hexagonal wurtzite ZnO. In addition to this, the interplanar distances 3.36 and 2.67 Å exhibited the (1 1 0) and (1 0 1) planes of rutile SnO_2 [35]. It is also observed that the small pores in the TEM morphology indicate the mesoporus nature of prepared nanocomposite. The detailed lattice structure of S-doped ZnO-SnO_2 was studied using HRTEM as shown Fig. 4e. The polycrystalline structure and good crystallization of S-doped ZnO-SnO_2 nanocomposite is observed in ring like SAED pattern (Fig. 4f). The smaller size provides higher surface area which effectively increases the photocatalytic activity of nanocomposite. The measured average particle size was found to be 30-40 nm (ZnO-SnO_2), 20-30 nm (B-doped ZnO-SnO_2), 10-20 nm (C-doped ZnO-SnO_2) and 5-10 nm (S-doped ZnO-SnO_2). Thus, the uniform spherical
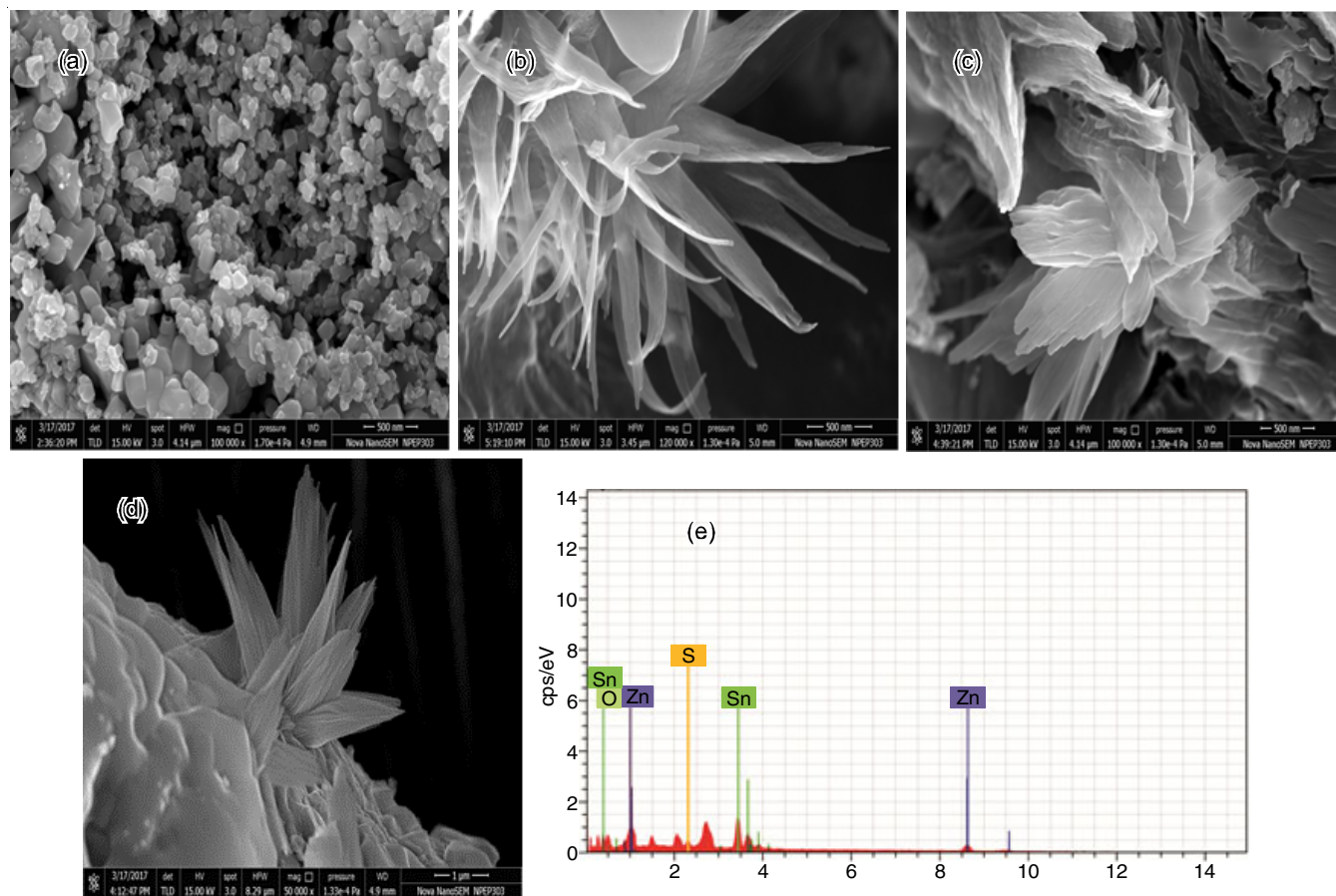
Fig. 3. FESEM images of (a) undoped ZnO-SnO$_2$, (b) B-doped ZnO-SnO$_2$, (c) C-doped ZnO-SnO$_2$, (d) S-doped ZnO-SnO$_2$ and (e) EDX spectrum of S-doped ZnO-SnO$_2$
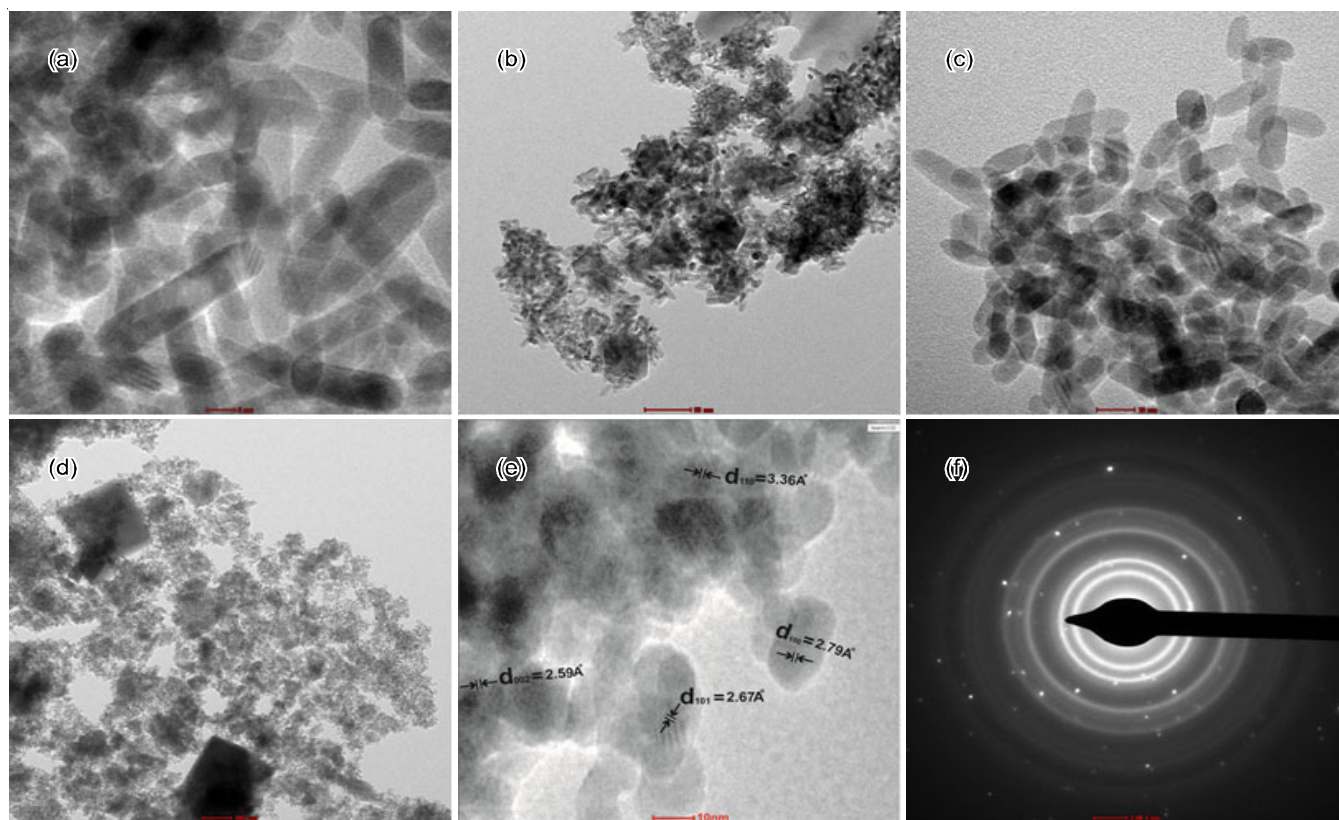

Fig. 4. TEM images of (a-b) undoped ZnO-SnO$_2$, (c) B-doped ZnO-SnO$_2$, (d) C-doped ZnO-SnO$_2$ and (e) HRTEM image and (f) SAED pattern of S-doped ZnO-SnO$_2$

morphology with least particle size was exhibited by S-doped ZnO-SnO$_2$. The obtained values are in good agreement with XRD study and those calculated using Scherrer's equation (Table-1).

XPS analysis: The surface structure and composition of synthesized S-doped ZnO-SnO$_2$ was investigated by XPS technique. Fig. 5a shows a high resolution XPS spectra of Sn3d. It displays symmetric spin orbital splitting of Sn3d$_{3/2}$ and Sn3d$_{5/2}$ at 486.7 and 495.1 eV, respectively and thus revealed the presence of SnO$_2$ crystals in the sample. The energy separation of these peaks (8.42 eV) is in line with the reported SnO$_2$ values [36]. The high resolution XPS spectrum for O1s peak can be deconvoluted into three main peaks at 530.1, 531.1 and 532.2 eV as shown in Fig. 5b). The lower peak at 530.1 eV indicates the Sn–O–Sn bonding and the middle peak at 531.1 eV attributes Sn–O–Zn bonding [37], while the peak at 532.2 eV is ascribed to adsorbed OH group [38]. In Fig. 5c, the high resolution XPS graph of S2p$_{3/2}$ show peak at 169.8 eV corresponding to S^{6+} states which indicates the successful doping of sulphur

atoms on the surface of ZnO-SnO$_2$ nanocomposites [39]. Two symmetric peaks for Zn2p orbital appeared at 1022.1 eV (Zn2p$_{3/2}$) and 1045.2 eV (Zn2p$_{1/2}$) confirmed the existence of normal oxidation state of Zn^{2+} in the sample (Fig. 5d) [40]. All these results points that the prepared photocatalyst is actually composed of ZnO and SnO$_2$ with sulphur doping.

UV-vis DR spectral analysis: The optical properties of prepared samples were studied by diffuse reflectance spectra as shown in Fig. 6. The prominent absorption edge of undoped ZnO-SnO$_2$ was estimated at 437 nm [41]. However, after non-metal doping the consistent red shift was observed. The prominent absorption at 437 nm was shifted towards the visible region with decrease in band gap energy. This decrease in band gap energy can be attributed to the synergistic effect of doped non-metal. The S-doped ZnO-SnO$_2$ nanocomposite shows absorption peak at 452 nm (increment of 15 nm) that exhibit the enhanced photocatalytic activity as compared to undoped ZnO-SnO$_2$. The absorption edge at higher wavelength in visible region indicates the more utilization of solar light for methyl
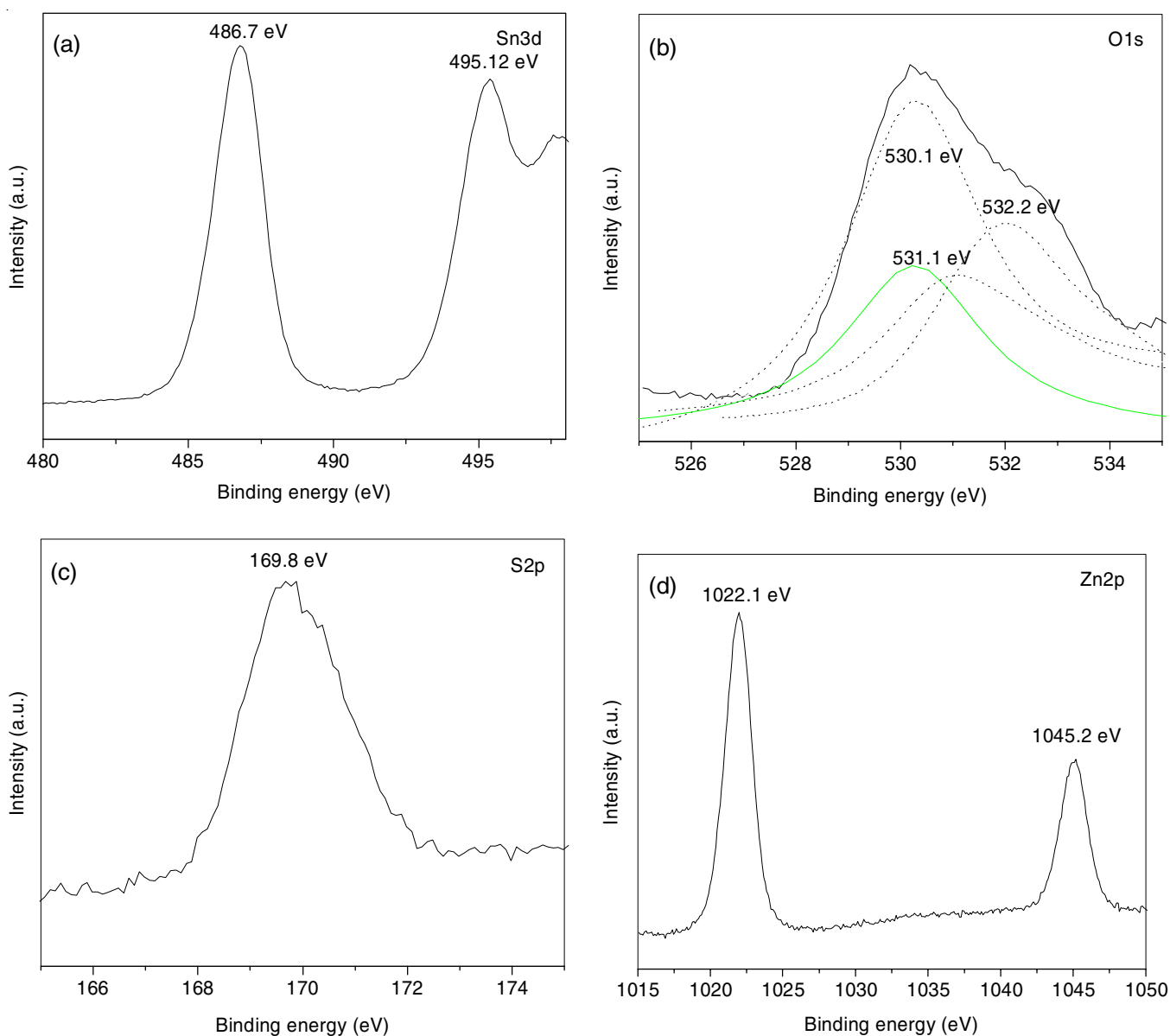

Fig. 5. High resolution XPS spectra of S-doped ZnO-SnO₂ (a) Sn3d5/2, Sn3d3/2, (b) O1s, (c) S$_{2p}$ and (d) Zn$_{2p}$
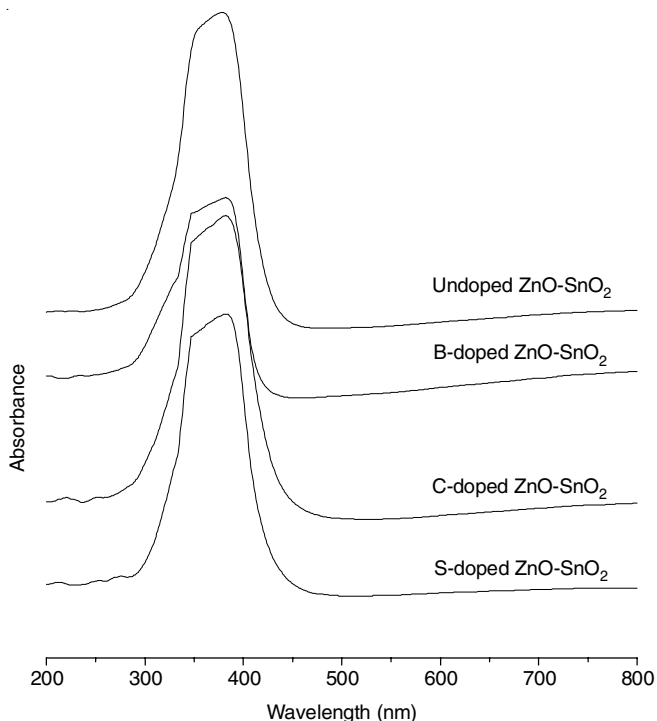
Fig. 6. UV-visible DRS of prepared photocatalysts

Fig. 7. Room temperature photoluminescence emission spectra of (a) undoped ZnO-SnO$_2$, (b) B-doped ZnO-SnO$_2$, (c) C-doped ZnO-SnO$_2$ and (d) S-doped ZnO-SnO$_2$

orange degradation. The band gap energy values of prepared photocatalysts were estimated using following equation:

$$\alpha(h\nu) = A(h\alpha - E_g)^{1/2}$$

where E_g, α, ν, h and A are the band gap energy (eV), absorption coefficient, frequency of light (s^{-1}), Planck's constant (6.626 $\times$ 10^{-34} m^{2}Kg/s) and a constant, respectively [42]. Thus the calculated band gap energies of undoped ZnO-SnO$_2$, B-ZnO-SnO$_2$, C-ZnO-SnO$_2$ and S-ZnO-SnO$_2$ are reported in Table-1.

Photoluminescence analysis: Photoluminescence (PL) measurements can be used to detect various fundamental material properties. In order to study the optical properties of prepared undoped and B/C/S-doped ZnO-SnO$_2$ nanocomposite photocatalysts were characterized by PL at room temperature (Fig. 7). Spectrum shows three emission bands in visible region at 414, 467 and 540 cm^{-1} from the transition in various kinds of defect states and oxygen vacancies in the nanocomposites [43]. The recombination of photoinduced e-h pair in the semiconductor is responsible for photoluminescence of photocatalyst and the intensity is directly proportional to the rate of e-h pair recombination. The intensity of PL peaks decreases from undoped ZnO-SnO$_2$ to B/C/S-doped ZnO-SnO$_2$. This result shows the lowest rate of e-h pair recombination in S-doped ZnO-SnO$_2$ nanocomposite. The doping of non-metal does not shift the emission of ZnO-SnO$_2$ nanocomposite but the decreases the PL intensity. This indicates that non-metal doping successfully suppresses e/h pair recombination.

Photocatalytic activity: The photocatalytic activity of undoped and B/C/S-doped ZnO-SnO$_2$ nanocomposite photocatalysts was studied by photodegradation experiment of methyl orange dye in aqueous solution under natural sunlight irradiation at λ_{max} 507 nm. Methyl orange dye is used as a representative of the organic pollutant to study the photodegradation ability of photocatalysts. Fig. 8 displays the comparison
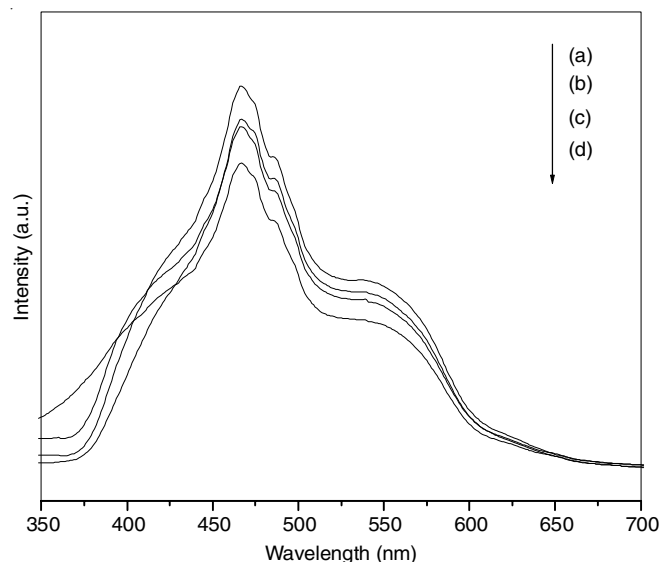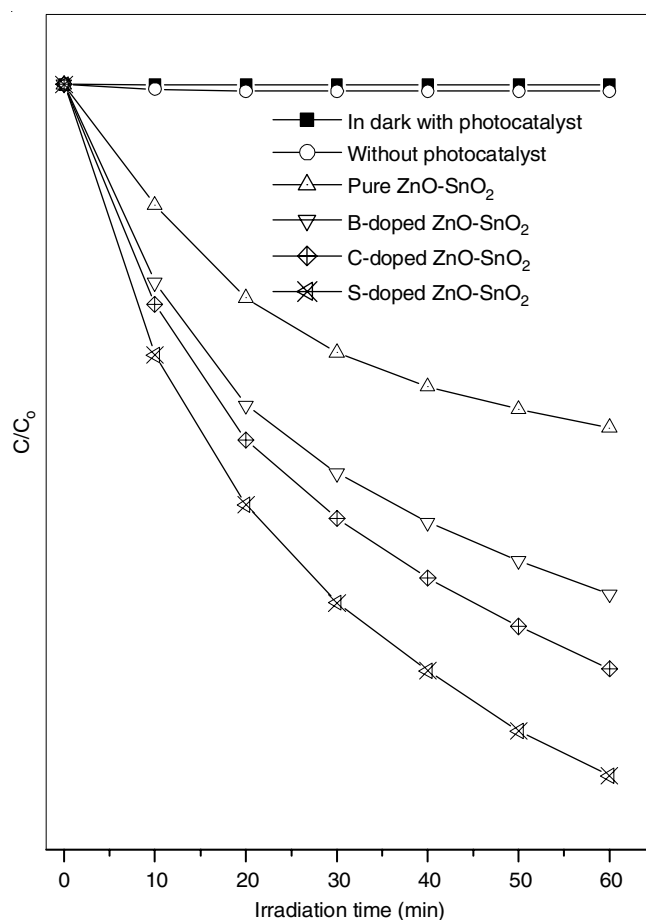
Fig. 8. Photocatalytic degradation of methyl orange over undoped and doped ZnO-SnO$_2$ under solar light irradiation

of the degradation of methyl orange by undoped and B/C/S-doped ZnO-SnO$_2$ photocatalysts. The dye degradation competency of the photocatalyst is defined in terms of C/C$_o$ where C$_o$ and C are the initial and reaction concentration of methyl orange after the equilibrium, respectively. The recorded photocatalytic activity both in dark as well as without addition of

photocatalyst revealed that methyl orange dye remains unreduced. It is well known that ZnO-SnO₂ photocatalysts has the dye degradation ability. Accordingly for ZnO-SnO₂, Fig. 8 shows 50 % methyl orange degradation after 60 min. It is worth to note that ZnO-SnO₂ exhibit enhanced dye degradation ability upon doping of boron, carbon and sulphur. Remarkable methyl orange degradation of about 99 % was recorded in case of S-doped ZnO-SnO₂ within the same period of time. The enhanced photodegradation efficiency of S-doped ZnO-SnO₂ can be attributed to the synergetic effect of low particle size, high surface area and low band gap energy of sulphur doping on ZnO-SnO₂ nanocomposites.

Mechanism for the enhanced photocatalytic activity: The schematic representation of solar photocatalytic methyl orange dye degradation using S-doped ZnO-SnO₂ photocatalyst is shown in Fig. 9. It is well known that the photocatalytic activity of ZnO-SnO₂ photocatalyst depends on its band alignment. The characterization results revealed the modified structure of ZnO-SnO₂ nanocomposite upon sulphur doping. When ZnO and SnO₂ form a heterojunction, due to their different work functions electrons are transferred from SnO₂ to ZnO. This transfer of electrons continues until the alignment of their Fermi levels. Thus, the attained thermal equilibrium forms a depletion layer at the interface.
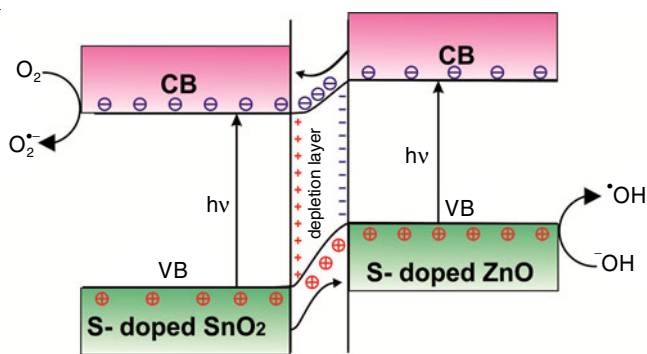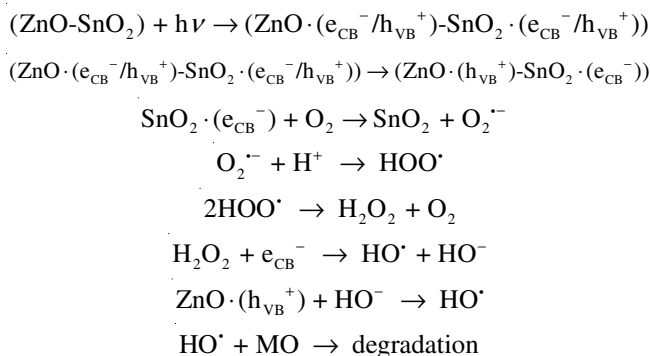

Fig. 9.   Schematic representation of methyl orange dye degradation using S-doped ZnO-SnO₂

The irradiation of solar light generates e/h pair in the photocatalyst. These photogenerated electrons get excited from valence band (VB) to conduction band (CB) in both ZnO and SnO₂ and create holes in the valence band. Further these electrons move from ZnO to SnO₂ (SnO₂ have lower CB than ZnO) and holes from SnO₂ to ZnO (ZnO have higher VB than SnO₂). Accordingly, the electrons get collected to SnO₂ and holes to ZnO due to the depletion layer induced by different work functions, which leads to enhancement in their lifetime due to decrease in e/h pair recombination. Further, adsorption of dissolved oxygen takes place on the surface of the photocatalyst. The electrons present in the conduction band of SnO₂ generate superoxide radical anions which on protonation convert to and finally generates radical. On the other side, the holes present in the valance band of ZnO with physisorbed water molecules create HO• radicals. It is well known that HO• radical is strong oxidizing agent and demineralize the organic molecules such as methyl orange. The proposed mechanism (**Scheme-I**) for degradation of methyl orange on the surface of S-doped ZnO-SnO₂ photocatalyst can be summarized as:

$$(ZnO\text{-}SnO_2) + h\nu \rightarrow (ZnO \cdot (e_{CB}^-/h_{VB}^+)\text{-}SnO_2 \cdot (e_{CB}^-/h_{VB}^+))$$

$$(ZnO \cdot (e_{CB}^-/h_{VB}^+)\text{-}SnO_2 \cdot (e_{CB}^-/h_{VB}^+)) \rightarrow (ZnO \cdot (h_{VB}^+)\text{-}SnO_2 \cdot (e_{CB}^-))$$

$$SnO_2 \cdot (e_{CB}^-) + O_2 \rightarrow SnO_2 + O_2^{\bullet -}$$

$$O_2^{\bullet -} + H^+ \rightarrow HOO^{\bullet}$$

$$2HOO^{\bullet} \rightarrow H_2O_2 + O_2$$

$$H_2O_2 + e_{CB}^- \rightarrow HO^{\bullet} + HO^-$$

$$ZnO \cdot (h_{VB}^+) + HO^- \rightarrow HO^{\bullet}$$

$$HO^{\bullet} + MO \rightarrow degradation$$

Scheme-I: Proposed mechanism for the methyl orange (MO) degradation on the surface of ZnO-SnO₂ photocatalyst

In addition to this increased e/h pair separation, the concomitant modifications in the structure of nanocomposite on sulphur doping contributes to enhanced photocatalytic activity. The sulphur doping enhances the photocatalytic efficiency mainly due to: (a) creation of more defects or oxygen vacancies in the crystal upon S-doping which can inhibit the recombination of the photoexcited charge carriers; (b) it also decreases the band gap and shifts the absorption towards visible light region. Also the formation of Sn–O–Zn bond, interfacial charge transfer and reduction in back reaction brings improvement in the lifetime of photoinduced charge carriers and their efficient separation. The interaction of doped sulphur with the photocatalyst (ZnO-SnO₂) efficiently creates the fitting environment for the generation of HO• and results in the enhanced photocatalytic efficiency.

Conclusion

To summarize, a new nanocrystalline undoped and B/C/S-doped ZnO-SnO₂ semiconductor with enhanced photocatalytic activity was successfully synthesized by simple precipitation method. It was found that, S-doped ZnO-SnO₂ shows increased photocatalytic activity as compared to undoped as well as B and C-doped ZnO-SnO₂ for the degradation of methyl orange dye under solar light. XPS study clearly showed the successful doping of sulphur on nanocomposite. The lowest rate of e-h pair recombination in S-doped ZnO-SnO₂ was confirmed by photoluminescence intensity measurement. All the doped nanocomposites exhibited red shift in DRS study with S-doped ZnO-SnO₂ being shifted more towards visible region. The improved photocatalytic activity of nanocomposites was attributed to least particle size, high BET surface area, low binding energy and overlapping of S2p orbital with the O2p orbital of ZnO and SnO₂. Present findings suggest the possible use of cheaper doping elements with enhanced photocatalytic activity for the degradation of methyl orange dye using solar light.

CONFLICT OF INTEREST

The authors declare that there is no conflict of interests regarding the publication of this article.

REFERENCES

1. S.C.R. Santos and R.A.R. Boaventura, *Appl. Clay Sci.*, **42**, 137 (2008); https://doi.org/10.1016/j.clay.2008.01.002.
2. M. Nocun, S. Kwasny, M. Kwasny and I. Grelowska, *J. Mol. Struct.*, **1167**, 194 (2018); https://doi.org/10.1016/j.molstruc.2018.04.095.
3. C. Karunakaran, V. Rajeswari and P. Gomathisankar, *Solid State Sci.*, **13**, 923 (2011); https://doi.org/10.1016/j.solidstatesciences.2011.02.016.
4. M. Qamar, Z.H. Yamani, M.A. Gondal and K. Alhooshani, *Solid State Sci.*, **13**, 1748 (2011); https://doi.org/10.1016/j.solidstatesciences.2011.07.002.
5. J. Cao, Y. Zhu, L. Shi, L. Zhu, K. Bao, S. Liu and Y. Qian, *Eur. J. Inorg. Chem.*, **2010**, 1172 (2010); https://doi.org/10.1002/ejic.200901116.
6. M. Shanmugam, A. Alsalme, A. Alghamdi and R. Jayavel, *ACS Appl. Mater. Interfaces*, **7**, 14905 (2015); https://doi.org/10.1021/acsami.5b02715.
7. E.J. Li, K. Xia, S.F. Yin, W.L. Dai, S.L. Luo and C.T. Au, *Mater. Chem. Phys.*, **125**, 236 (2011); https://doi.org/10.1016/j.matchemphys.2010.09.013.
8. L.S. Zhong, J.S. Hu, H.P. Liang, A.M. Cao, W.G. Song and L.J. Wan, *Adv. Mater.*, **18**, 2426 (2006); https://doi.org/10.1002/adma.200600504.
9. P. Manjula, R. Boppella and S.V. Manorama, *ACS Appl. Mater. Interfaces*, **4**, 6252 (2012); https://doi.org/10.1021/am301840s.
10. C.S. Lee, I.D. Kim and J.H. Lee, *Sens. Actuators B: Chem.*, **181**, 463 (2013); https://doi.org/10.1016/j.snb.2013.02.008.
11. A.B. Gambhire, M.K. Lande, S.B. Kalokhe, M.D. Shirsat, K.R. Patil, R.S. Gholap and B.R. Arbad, *Mater. Chem. Phys.*, **112**, 719 (2008); https://doi.org/10.1016/j.matchemphys.2008.06.022.
12. T. Ohno, F. Tanigawa, K. Fujihara, S. Izumi and M. Matsumura, *J. Photochem. Photobiol. Chem.*, **118**, 41 (1998); https://doi.org/10.1016/S1010-6030(98)00374-8.
13. L.N. Moghadam and M.S. Niasari, *J. Mol. Struct.*, **1146**, 629 (2017); https://doi.org/10.1016/j.molstruc.2017.06.038.
14. H.S. Woo, C.W. Na, I.D. Kim and J.H. Lee, *Nanotechnology*, **23**, 245501 (2012); https://doi.org/10.1088/0957-4484/23/24/245501.
15. B. Pal, M. Sharon and G. Nogami, *Mater. Chem. Phys.*, **59**, 254 (1999); https://doi.org/10.1016/S0254-0584(99)00071-1.
16. Y.J. Chiang and C.C. Lin, *Powder Technol.*, **246**, 137 (2013); https://doi.org/10.1016/j.powtec.2013.04.033.
17. S.A. Mahmoud and O.A. Fouad, *Sol. Energy Mater. Sol. Cells*, **136**, 38 (2015); https://doi.org/10.1016/j.solmat.2014.12.035.
18. J. Xu, Y. Ao, M. Chen and D. Fu, *J. Alloys Compd.*, **484**, 73 (2009); https://doi.org/10.1016/j.jallcom.2009.04.156.
19. R. Marschall and L. Wang, *Catal. Today*, **225**, 111 (2014); https://doi.org/10.1016/j.cattod.2013.10.088.
20. L. Xu, E.M.P. Steinmiller and S.E. Skrabalak, *J. Phys. Chem. C*, **116**, 871 (2012); https://doi.org/10.1021/jp208981h.
21. V. Kumar, A. Govind and R. Nagarajan, *Inorg. Chem.*, **50**, 5637 (2011); https://doi.org/10.1021/ic2003436.
22. H.F. Yu, *J. Mater. Res.*, **22**, 2565 (2007); https://doi.org/10.1557/jmr.2007.0316.
23. T. Umebayashi, T. Yamaki, H. Itoh and K. Asai, *Appl. Phys. Lett.*, **81**, 454 (2002); https://doi.org/10.1063/1.1493647.
24. G. Yang, T. Xiao, J. Sloan, G. Li and Z. Yan, *Chem. Eur. J.*, **17**, 1096 (2011); https://doi.org/10.1002/chem.201001676.
25. P. Xu, J. Lu, T. Xu, S. Gao, B. Huang and Y. Dai, *J. Phys. Chem. C*, **114**, 9510 (2010); https://doi.org/10.1021/jp101634s.
26. N.O. Gopal, H.H. Lo and S.C. Ke, *J. Am. Chem. Soc.*, **130**, 2760 (2008); https://doi.org/10.1021/ja711424d.
27. P. Periyat, D.E. McCormack, S.J. Hinder and S.C. Pillai, *J. Phys. Chem. C*, **113**, 3246 (2009); https://doi.org/10.1021/jp808444y.
28. R. Lamba, A. Umar, S.K. Mehta and S.K. Kansal, *J. Alloys Compd.*, **620**, 67 (2015); https://doi.org/10.1016/j.jallcom.2014.09.101.
29. R. Lamba, A. Umar, S.K. Mehta and S.K. Kansal, *Talanta*, **131**, 490 (2015); https://doi.org/10.1016/j.talanta.2014.07.096.
30. L. Ma, S.Y. Ma, H. Kang, X.F. Shen, T.T. Wang, X.H. Jiang and Q. Chen, *Mater. Lett.*, **209**, 188 (2017); https://doi.org/10.1016/j.matlet.2017.08.004.
31. R. Lamba, A. Umar, S.K. Mehta and S.K. Kansal, *J. Alloys Compd.*, **653**, 327 (2015); https://doi.org/10.1016/j.jallcom.2015.08.220.
32. S. Zhuang, X. Xu, B. Feng, J. Hu, Y. Pang, G. Zhou, L. Tong and Y. Zhou, *ACS Appl. Mater. Interfaces*, **6**, 613 (2014); https://doi.org/10.1021/am4047014.
33. J.H. Xu, J. Li, W.L. Dai, Y. Cao, H. Li and K. Fan, *Appl. Catal. B*, **79**, 72 (2008); https://doi.org/10.1016/j.apcatb.2007.10.008.
34. M.T. Uddin, Y. Nicolas, C. Olivier, T. Toupance, L. Servant, M.M. Müller, H.J. Kleebe, J. Ziegler and W. Jaegermann, *Inorg. Chem.*, **51**, 7764 (2012); https://doi.org/10.1021/ic300794j.
35. Q. Ge, S.Y. Ma, Y.B. Xu, X.L. Xu, H. Chen, Z. Qiang, H.M. Yang, L. Ma and Q.Z. Zeng, *Mater. Lett.*, **191**, 5 (2017); https://doi.org/10.1016/j.matlet.2016.12.116.
36. M. Faisal, A.A. Ibrahim, F.A. Harraz, H. Bouzid, M.S. Al-Assiri and A.A. Ismail, *J. Mol. Catal. A: Chem.*, **397**, 19 (2015); https://doi.org/10.1016/j.molcata.2014.10.027.
37. X. Jia, Y. Liu, X. Wu and Z. Zhang, *Appl. Surf. Sci.*, **311**, 609 (2014); https://doi.org/10.1016/j.apsusc.2014.05.118.
38. J. Mu, C. Shao, Z. Guo, Z. Zhang, M. Zhang, P. Zhang, B. Chen and Y. Liu, *ACS Appl. Mater. Interfaces*, **3**, 590 (2011); https://doi.org/10.1021/am101171a.
39. D.I. Sayago, P. Serrano, O. Bohme, A. Goldoni, G. Paolucci, E. Roman and J.A. Martin-Gago, *Phys. Rev. B*, **64**, 205402 (2001); https://doi.org/10.1103/PhysRevB.64.205402.
40. L. Zheng, Y. Zheng, C. Chen, Y. Zhan, X. Lin, Q. Zheng, K. Wei and J. Zhu, *Inorg. Chem.*, **48**, 1819 (2009); https://doi.org/10.1021/ic802293p.
41. W.W. Wang, Y.J. Zhu and L.X. Yang, *Adv. Funct. Mater.*, **17**, 59 (2007); https://doi.org/10.1002/adfm.200600431.
42. E.A. Davis and N.F. Mott, *Philos. Mag.*, **22**, 0903 (1970); https://doi.org/10.1080/14786437008221061.
43. M.A. Gondal, Q.A. Drmosh and T.A. Saleh, *Appl. Surf. Sci.*, **256**, 7067 (2010); https://doi.org/10.1016/j.apsusc.2010.05.027.